Functionalization of phosphocalcic bioceramics for bone repair applications

Chantal Damia, David Marchat, Charly Lemoine, Nathalie Douard, Vincent Chaleix, Vincent Sol, Nathanael Larochette, Delphine Logeart-Avramoglou, Joël Brie, Eric Champion

Chantal Damia, David Marchat, Charly Lemoine, Nathalie Douard, Vincent Chaleix, et al.. Functionalization of phosphocalcic bioceramics for bone repair applications. Materials Science and Engineering: C, 2019, 95, pp.343-354. 10.1016/j.msec.2018.01.008 . hal-02080103

Functionalization of phosphocalcic bioceramics for bone repair applications

Authors : Chantal Damia [a], David Marchat [b], Charly Lemoine [a], Nathalie Douard [b], Vincent Chaleix [c], Vincent Sol [c], Nathanaël Larochette [d], Delphine Logeart-Avramoglou [d], Joël Brie [a,e], Eric Champion [a]

Affiliations:

a : Univ. Limoges, CNRS, IRCER, UMR 7315, F-87000 Limoges, France

b :Ecole Nationale Supérieure des Mines, CIS-EMSE, INSERM U1059, 158 cours Fauriel, F-42023 Saint-Etienne cedex 2, France

c:Univ. Limoges, LCSN EA 1069, F-87000 Limoges, France

d:Laboratory of Bioengineering and Bioimaging for Osteo-Articular tissues, UMR 7052, CNRS, Paris Diderot University, Sorbonne Paris Cité, Paris, France

e :CHU Limoges, Service de Chirurgie Maxillo-Faciale, F-87000, Limoges, France

Key words: Silicate-substituted hydroxyapatite; Sphere elaboration; Surface functionalization; BMP-2

Abstract: This work is devoted to the processing of bone morphogenetic protein (BMP-2) functionalized silicate substituted hydroxyapatite (SiHA) ceramic spheres. The motivation behind it is to develop injectable hydrogel/bioceramic composites for bone reconstruction applications. SiHA microspheres were shaped by spray drying and thoroughly characterized. The silicate substitution was used to provide preferred chemical sites at the ceramic surface for the covalent immobilization of BMP-2. In order to control the density and the release of the immobilized BMP-2, its grafting was performed via ethoxysilanes and polyethylene glycols. A method based on Kaiser's test was used to quantify the free amino groups of grafted organosilanes available at the ceramic surface for BMP-2 immobilization. The SiHA surface modification was investigated by means of X-ray photoelectron spectroscopy, Fourier transformed infrared spectroscopy and thermogravimetry coupled with mass spectrometry. The BMP-2 bioactivity was assessed, in vitro, by measuring the luciferase expression of a stably transfected C3H10 cell line (C3H10-BRE/Luc cells). The results provided evidence that the BMP-2 grafted onto SiHA spheres remained bioactive.

Introduction:

The reconstruction of bone defects resulting from trauma, malformations, cancer or other pathologies such as osteomyelitis remains a significant clinical issue. The current approaches include autografts, allografts or synthetic biomaterials but none of them are really satisfactory. Bone autograft is considered as the gold standard in the domain of bone substitution because it contains the necessary components for the bone induction and growing: extracellular matrix, growth factors and osteocompetent cells. However harvesting autologous bone tissue induces medical complications (pain, infection, hemorrhage, morbidity), as shown by reported complications ranging from 2.8% to 49% of clinical cases [1]. Furthermore, the limited amounts of autograft bone available as well as an excessive graft resorption may make their use impossible. Alternatively, allografts can be used but they can transmit infectious diseases [2]. Besides, the architecture (shape and size) of such implants is often unsatisfying because it cannot be adapted to the bone defect. First (i.e. bioinert) and second (i.e. bioactive) generation of synthetic biomaterials have been developed for the filling of bone defects [3]. Among them, calcium phosphate ceramics (CPCs), such as hydroxyapatite (HA) $Ca_{10}(PO_4)_6(OH)_2$, have been used since the early 1980s [4]. Due to a chemical composition close to the bone mineral, they are highly biocompatible. They are also osteoconductive [5], but not or weakly osteoinductive [6]. Depending on the size and geometry of the defects, CPCs, in the form of either massive macroporous scaffolds or granules, are implanted [[7], [8], [9]]. Hence, the new bone tissue grows from the host bone and penetrates within the interconnected macropores network of scaffolds or within the interstitial voids between granules. However this bone ingrowth only occurs up to about 1 cm from the bone apposition and therefore full bone repair is restricted to defects of small dimensions [10]. The osteogenesis must be stimulated in order to extend applications of porous HA ceramics to the repair of large osseous defects. For these reasons, researchers aim to develop a new generation (the third one) of synthetic bioceramics able to induce both bone formation (i.e. osteoinductive) and angiogenesis [3,6]. To this end, the combination of biomolecules or growth factors, known for their activity on bone formation, with HA ceramics appears as a promising strategy to enhance the biological performances of implants [11]. Adsorption or covalent grafting of such biomolecules on HA surface could enhance both osseointegration and osteoinduction of implants but there is still an overall lack of success in bringing this technology to the clinic, especially for use in restoring large bone defects [12,13]. Among the biomolecules of interest for bone healing [14], bone morphogenetic protein-2 (BMP-2) is a good candidate as it is a key factor of the signaling cascade that governs fracture repair [15]. It induces early stage proliferation and differentiation of osteoprogenitor cells [16,17], and markedly stimulates proliferation of periosteal cells in vitro [18,19]. It was also shown that BMP-2 is involved in vasculogenesis and angiogenesis [20,21].

Due to its high osteoinductivity in vivo, recombinant human BMP-2 (rh-BMP-2) has been introduced in human clinical practice in 2003 for the repair of delayed- or non-unions. Despite its efficacy, several concerns have been raised recently regarding the occurrence of adverse effects of BMP-2 such as ectopic ossification, inflammatory reaction and pain [[22], [23], [24], [25], [26]]. The main reason for these effects is the use of supraphysiological dose of BMP-2 (e.g. several milligrams). The collagen sponge or paste currently used as BMP carrier in daily routine does not allow controlling the growth factor delivery [27] and there is a need to engineer new delivery systems for BMP-2 [28]. In an effort to reduce the protein diffusion and to increase its residence and activity time, current research endeavors to graft BMP-2 at the carrier surface. Recent studies demonstrate the feasibility of enhancing implant osseointegration and gap bridging by covalently immobilized rh-BMP-2 on titanium and polymer implant surfaces [29,30]. The described grafting increases the half-life of rh-BMP-2 up to 40–60 days (half-life of rh-BMP-2 is approximately 2.5 days in vivo [31]) and allows controlling the sustained release of rh-BMP-2 with a high level of biological activity. Mercado et al. provided evidence that rh-BMP-2 grafted to biodegradable polymer nanoparticles was, after 14 days, as effective in inducing mineralization as the native rh-BMP-2 [30].

The objective of the present study was to develop HA ceramic medical devices functionalized by BMP-2, exhibiting osteoinductive properties, for bone tissue engineering. The choice of a carrier with the most appropriate design and chemical composition for such grafting is essential. Spherical granules should provide an adapted surgical solution for the filling and repair of bone defects with complex shape. Such spheres of controlled size, density and chemistry appear as a right filler in injectable composite hydrogel/CPC for bone reconstruction applications [32]. Indeed, this combination was proved to be more efficient than hydrogel polymers or calcium phosphates granules alone [33,34]. Moreover, this type of composite was found to be a suitable injectable bone cell carrier [35].

Regarding the chemical composition, bio-available silicon species were reported to play an important role in bone growth processes [[36], [37], [38]]. They stimulate spontaneous calcium phosphate precipitation [39], increase bone mineral density [40] and have a role in collagen synthesis and matrix mineralization [38,41], [40]. The incorporation of silicon in the HA structure was thus expected to be a solution for improving HA bioactivity [42]. Despite conflicting conclusions about the origin of the enhanced bioactivity of silicate-substituted hydroxyapatites (SiHA) compared to HA [[43], [44], [45]], SiHA ceramic implants were shown to be efficient in vivo [46,47]. The synthesis of SiHA, (Ca10(PO4)6−y(SiO4)y(OH)2−y), usually using aqueous precipitation, has been published by several teams [[48], [49], [50]]. Moreover we have shown in previous studies that it is possible to produce biocompatible ceramics made of single phase SiHA [51,52]. Additionally, silicate-substituted ceramics could also be used to provide preferential sites on the ceramic surface for controlled immobilization of BMP-2 via Si-O-Si covalent bonding with organosilane and for its further sustained release. Indeed, the method of silanisation is often used to functionalize the HA surface with covalently grafted biomolecules [[53], [54], [55], [56]] and APTES (3-aminopropyltriethoxysilane) is classically employed for the silanisation of HA [[55], [56], [57], [58]]. Its three siloxane functions (R′-O-Si) can lead to organic-inorganic bonds and its terminal amine allows further reactions. Therefore, APTES acts as an anchor. The bond between the anchor and a biomolecule is complex; the use of a cross-linker agent with suitable functions is required to link the substrate after silanisation to the biomolecules [56,57] and to provide a minimum distance for cell binding process [59,60].

Based on these previous studies and hypotheses, the present work was devoted to the processing and characterization of spheres of SiHA ceramic functionalized by controlled immobilization of recombinant rh-BMP-2 via organic intermediates.

Materials and Methods:

Elaboration of SiHA ceramics:

Silicate-substituted hydroxyapatite (SiHA) powders were first synthesized based on a previously published aqueous precipitation method [52]. Briefly, a calcium nitrate solution (Ca(NO3)2.4H2O, 99% pure, Merck, Germany, [Ca] = 3.04 mol/L) was added dropwise, using a peristaltic pump (25 mL/min), to a diammonium hydrogen phosphate aqueous solution ((NH4)2HPO4, 99% pure, Merck, Germany, [P] = 2.56 mol/L) previously mixed with an alkaline silicate solution ([Si] = 39.0 ± 0.5 mmol/L). The latter was prepared according to a protocol detailed elsewhere [52]. The reaction was performed under stirring (500 rpm) and bubbling of inert gas (5 mL/min, Argon, 4.8, AirLiquide, France,). Reagents ratio were calculated according to the theoretical formula Ca10(PO4)5.6(SiO4)0.4(OH)1.6. Precipitation was performed at 50 °C and a pH value of 10.80 ± 0.05. The pH of the suspension was adjusted by the addition of 28% ammonia solution (Merck, Germany) by means of a dosing pump (ProMinent, England) coupled with a pH controller (Mettler Toledo M400, United States) and a pH-electrode (Mettler Toledo Inpro®4800/120/PT100, United States). The temperature was controlled and regulated automatically with an external T-probe. After complete introduction of the calcium nitrate solution, the suspension was matured for 20 ± 2 h, and then centrifuged at 4500 rpm for 10 min (ThermoFisher Scientific, Sorvall™ Legend XF). Cakes were then dried at 80 °C for 24 h, and finally grinded in absolute ethanol (H3CCH2OH, >99,5%, VWR, Germany) by means of a planetary ball miller (PM400, Retsch, Germany) with zirconium oxide jars and balls.

Before shaping microspheres, SiHA raw powder was heat-treated at 1000 °C for 2 h in order to adjust its specific surface area (SBET) at 8.5 ± 0.5 m^2/g. Micrometric spheres of SiHA were manufactured by means of a Büchi spray dryer B-290 equipped of a two-fluid spray nozzle. SiHA slurry was first prepared by blending 60.0% (w/w) of powder, 38.9% (w/w) of pure water, and 1.1% (w/w) of dispersing agent (Darvan C-N, R. T. Vanderbilt Company Inc., USA) for 1 h at 45 rpm in an alumina jar with alumina beads of 10 mm diameter (Tosoh, 99.5%, Japan). This slurry was fed into the spray nozzle with a flow of 3 mL/min and sprayed out with a nitrogen flow of 350 mL/min. The formed aerosol droplets were then dried in an air gas flow of 20 m3/h maintained at 190 °C (inlet temperature). Dried SiHA spheres were further sintered at 1140 °C for 1 h under steam (pH20 = 286 mbar) after a debinding step (1 °C/min up to 450 °C). Finally, the sintered spheres were sieved and the portion between 25 µm and 50 µm was collected for the study. In order to perform complementary thermal analyses, SiHA pellets were formed by pressing 450 mg of SiHA powder (specific area of 30 m2/g) at 50 MPa in a 12.6 mm diameter stainless steel die (LLOYD Instruments, LR50K, UK). This uniaxial pressing was followed by a cold isostatic pressing under 3000 MPa (Nova Swiss, Switzerland). Finally, after sintering at 1140 °C for 2 h under air, pellets were mirror polished (edge and surface) with successive diamond pastes to a 1 µm finish (Mecapol P320, PRESI, France).

Functionalisation of SiHA spheres

Surface modification of SiHA spheres using a grafting-from approach is summarized in Fig. 1. Firstly, the SiHA spheres were silanised with APTES (3-aminopropyltriethoxysilane, $NH_2(CH_2)_3Si(OCH_2CH_3)_3$) in order to have free amine groups on their surface (Step 1). Then, NHS-PEG$_6$-maleimide (succinimidyl-[(*N*-maleimidopropionamido)-hexaethyleneglycol] ester) was added *via* a specific reaction between the terminal amine groups of APTES and succinimidyl (NHS) functions (Step 2). Finally the BMP-2, previously functionalized with Traut's reagent [61], was linked to NHS-PEG$_6$-maleimide by specific click-thiol-ene reaction (Step 3).

Before the silanisation, the substrates were dried at 110 °C for 3 h in an oven. SiHA spheres (1.30 ± 0.01 g) and 20 mL of anhydrous toluene (Sigma Aldrich, purity: 99.8%) were introduced in a 100 mL Schlenk round bottom flask. When the temperature reached 60 °C, APTES (Sigma Aldrich, purity ≥98%, noted T) was added dropwise to prevent clumping [62]. The final silane concentration in the media was 0.20 ± 0.06 mol/L which corresponded to a large excess of silane. The media was refluxed 3 h at 90 °C and then maintained at 60 °C for 12 h. The reaction was conducted under Ar atmosphere and electromagnetic stirring. The APTES-functionalized SiHA spheres (SiHA-T) were rinsed three times using first toluene (two washes) and then technical ethanol (one wash) (96%, VWR, Germany). They were dried at 100 °C overnight in an oven and under vacuum for 3 h. Primary amine sites of SiHA-T pellets were quantified by Ultraviolet-Visible (UV-Vis) photometric methods [63]. The results highlighted a density dNH2 of 7.0 × 10−6 ± 0.5 × 10−6 mol/m2.

NHS-PEG6-maleimide (Thermo scientific, 1.3 equivalent, 4.30 mL of a 5.34 mM solution in anhydrous DMSO, 2.3 × 10−5 mol) were added to 15 mL of a phosphate-buffered saline solution (PBS 10× pH 7.4 solution, Alfa Aeser) containing 1.07 g of SiHA-T spheres (dNH2 = 7.0 × 10−6 ± 0.5 × 10−6 mol/m2, SBET = 2.42 m2/g). The mixture was carefully stirred at RT during 24 h and under Ar atmosphere. The PEG-maleimide-functionalized SiHA-T spheres (SiHA-PEG) were rinsed three times using first PBS 10X (two washes) and then technical ethanol (one wash).

2-iminothiolane hydrochloride (i.e. Traut's reagent, ≥98, Sigma-Aldrich, 20 equivalent, 261 µL of 14 mM a solution in milliQ water, 3.0 × 10−6 mol) was added to rh-BMP-2 (InductOs®, Medtronic BioPharma B·V, 4.9 mL of a 0.78 mg/mL solution of rh-BMP-2, 1.47 × 10−7 mol, MBMP-2 = 26,000 kDa). After 1 h of reaction, the mixture was centrifuged three times at 4000 rpm in Amicon Ultra-4 10K1 ultrafiltration tubes to remove the excess of Traut's reagent. Thiolated rh-BMP-2 (0.008 equivalent, 750 µL of a 5.10 mg/mL solution, 1.47 × 10−7 mol) was then added to a PBS 10X pH 7.4 solution (15 mL) containing 1.04 g of SiHA-PEG spheres (dNH2 = 7.0 × 10−6 ± 0.5×10−6 mol/m2, SBET = 2.42 m2/g). The mixture was carefully stirred at RT during 24 h and under Ar atmosphere. The obtained SiHA-BMP-2 spheres were rinsed two times using PBS 10X and lyophilized. SiHA pellets were functionalized in the same way as spheres.

Characterizations

Crystalline phases were identified by means of a Siemens D5000 θ/2θ X-ray diffractometer (XRD) using CuKα radiation and operating at 40 kV and 20 mA. XRD patterns were collected over a 2θ range of 10–120° at a step size of 0.02° with a counting time of 15 s per step. Crystalline phases were identified by comparison with reference patterns in ICDD-PDF (International Centre for Diffraction Data – Powder Diffraction Files). Diffractrograms were also used to calculate the lattice parameters of SiHA spheres. The position and intensities of the lines were adjusted by the refinement program. The refinements were performed using the space group of the HA structure $P6_{3/m}$ (ICDD-PDF: 09-432) and the Le Bail algorithm implemented in the Topas software (Bruker, Germany). The initial cell parameters were set to $a = 9.418$ Å and $c = 6.884$ Å.

The grinded spheres were also analyzed by Fourier transform infrared (FTIR) spectroscopy using a Bruker VERTEX 70 spectrometer (Bruker Optics, France), equipped with a monolithic diamond ATR crystal (Quest ATR diamond, Specac, USA). The spectra were recorded from 4000 to 400 cm^{-1} at a resolution of 2 cm^{-1} and obtained by signal averaging of 64 successive scans. Spectra of functionalized substrates were realized with concentrated powders (2.8% w/w in KBr matrix) on a Spectrum One (Perkin-Elmer). They were collected in the range of 4000–400 cm^{-1} with a resolution of 2 cm^{-1}. Spectra were normalized with respect to the ν_4 PO_4 band at 602 cm^{-1} [64].

The silicon content in powders was determined by inductively coupled plasma atomic emission spectrometry (ICP/AES) (HORIBA Spectrometer, Jobin-Yvon, Activa model). A mass of 250 mg of powder was dissolved in a nitric acid aqueous solution (0.2 M) in 100 mL calibrated flask.

Scanning Electron Microscopy (SEM, JEOL JSM-6500F, USA) was used to image the morphology of the spheres. Powder samples were deposited on a carbon-coated film and sputtered with approximately 20 nm of gold prior to imaging (Quorum, Q150RES, England).

The shape of the spheres and their surface porosity were quantified from SEM images using the ImageJ software (National Institutes of Health, USA). The minimum (xF,*min)* and maximum *(*xF,*max)* Feret diameter were evaluated for both; xF,*min* corresponding to the shortest Feret Diameter and xF,*max* to the longest Feret diameter for one sphere or one pore. Three morphological factors, aspect ratio (*A.R.*), form factor (*F.F.*), and roundness (*R.*) were calculated to characterize the spheres shape from the following equations and in accordance with the ISO norm 9276–6:

$$A.R. = \frac{xF,\mathrm{min}}{xF,\mathrm{max}} \tag{1}$$

$$F.F. = \sqrt{\frac{4\times\pi\times A}{P^2}} \tag{2}$$

$$R. = \sqrt{\frac{4\times A}{\pi\times \mathrm{xF,max}^2}} \tag{3}$$

with A and P the cross-sectional area and the perimeter of the spheres, respectively. The theoretical values of the morphological factors *A.R.*, *F.F.* and *R.* are equal to 1 for a circle. These analyses were performed on $N = 29$ spheres.

The absolute density of the SiHA powder was determined by helium pycnometry measurements using a Micromeritics Accupyc 1330 apparatus. Specific surface area (S_{BET}) of the SiHA powders and spheres were determined on samples that were outgassed at 200 °C for 8 h using the Brunauer-Emmett-Teller (BET) 5-points method

($N = 4$) using the N_2 adsorption isotherm (Micromeritics ASAP 2010, Germany).

X-ray photoelectron spectroscopy (XPS) acquisitions were realized with a Kratos Axis Ultra spectrometer using a monochromatic source Al Kα (180 W). The analyzed area was 300 × 700 μm, the pass energy was 160 eV for the surveys (step size of 0.5 eV) and 20 eV for the high-resolution spectra (step size of 0.1 eV). The process has an associated error of ±0.2 eV. Peak positions were referenced to the Ca2p⅔ at 347.0 eV and a flood gun was used for charge compensation. After a background correction by the Shirley method, the decomposition of the spectra was carried out using the CasaXPS software (Casa Software Ltd) and the atomic composition of each sample was calculated using the Kratos/PHi/Wagner RSF (Relative Sensitivity Factors).

Thermogravimetry analyses coupled with mass spectroscopy (TG/MS) from 30 °C to 1300 °C were performed under He atmosphere (20 mL/min). The gases released during the heat treatment from mass 1 to 201 were analyzed by a quadrupole residual gas analyzer (Pfeiffer Vacuum Thermostar) with an ion-beam of 15 eV. The SiHA spheres were analyzed with a heating rate of 20 °C/min on a thermobalance (STA 449 F3, Netzsch) coupled to the MS apparatus. To increase the definition of the measurement the TG analysis of the SiHA pellets were performed at 30 °C/min on a Setsys Evolution TGA device and the MS data were obtained during a heat treatment at 5 °C/min. Whatever the sample, the mass was around 30 mg with a precision of 0.001 mg.

Biological activity of grafted BMP-2

The BMP-2 bioactivity was assessed by measuring the luciferase expression of a stably transfected C3H10 cell line (C3H10-BRE/Luc cells), which was transfected with a bone-responsive element (BRE) fused to the firefly luciferase reporter gene (BRE-Luc). The addition of BMP-2 (1–50 ng/mL) to C3H10-BRE/Luc cells resulted in a dose-dependent increase in luciferase activity in cell lysates [65]. Briefly, 40,000 C3H10-BRE/Luc cells were seeded with various (1, 2.5 and 5 mg) amounts of SiHA-BMP-2 spheres. They were put in a plate featuring 48 wells filled with an alpha-modified Eagle medium (Sigma) supplemented with 10% fetal calf serum (FCS) and antibiotics (all chemicals from the PAA Laboratories). Then they were cultured under standard cell culture conditions and after 24 h of incubation, cell lysis and luciferase measurements were carried out as previously described [65]. Measurements were normalized to the DNA content of each sample as measured by the CyQuant assay (Thermo Fisher Scientific). The level of luciferase expression induced by the grafted BMP-2 was compared with the following control preparations: C3H10-BRE/Luc cells incubated with 10 mg of uncoated SiHA spheres (negative control) as well as soluble BMP-2 in the culture medium (positive controls).

Results

SiHA spheres analysis

Fig. 2 shows the XRD diffractogram and FTIR spectrum of SiHA powder, centered on the range $20 \geq 2\theta \geq 50°$ and $1200 \geq \nu \geq 500$ cm−1, respectively. The XRD pattern exhibits only the characteristic diffraction lines of hydroxyapatite (HA, PDF 9-432), and the FTIR spectrum shows only the vibration modes which are characteristic of SiHA [52]. The a and c lattice parameters are equal to 9.426 ± 0.001 Å and 6.895 ± 0.001 Å, respectively, and are equivalent to already published values [52]. The unit cell volume is thus equal to 530.1 ± 0.1 Å3. The SiHA powder is pure and monophasic. Elemental analysis indicates that the SiHA powder is composed of 1.14 ± 0.05% (w/w) of silicon corresponding to y = 0.41 ± 0.02 mol in the chemical formula $Ca_{10}(PO_4)_6$−y(SiO_4)y(OH)y and to a molar mass of 996.6 ± 0.4 g/mol. The theoretical density of the material is thus equal to 3.12 g/cm3 by combining these results through the Eq. (4).

$$\rho = \frac{M_{SiHA}}{V \times N} \qquad (4)$$

with ρ the volumetric mass density (g/cm3); MSiHA the SiHA molar mass (g/mol), V the unit cell volume (cm3), and N the Avogadro number (6.0221 × 1023 mol−1). This theoretical density is equivalent to the absolute density determined by helium pycnometry: 3.1 ± 0.3 g/cm^3.

SEM images of the SiHA powder are presented on Fig. 3. The shape factors A.R., F.F., and R. were evaluated at 1.04 ± 0.03, 0.90 ± 0.05 and 0.98 ± 0.02, respectively, for particles diameter ranging from 70 μm down to 22 μm. SEM image analysis also estimates the porosity at 8 ± 2%, and the mean xF,min and xF,max of the surface pores at 0.26 ± 0.12 μm and 0.50 ± 0.22 μm, respectively (with the lowest xF,min = 0.13 μm and the highest xF,max = 1.45 μm). These results prove that the powder is composed of spherical porous aggregates. Finally, the SBET is equal to 2.42.0 ± 0.03 m^2/g.

Characterization of functionalized SiHA spheres

Fig. 4 presents the FTIR spectra of the functionalized SiHA spheres. All the samples contained absorbed water (νH2O at 3430 cm−1). The first zoom (interval 3200–2700 cm−1) highlights bands which are not present on the SiHA spectrum, at 2973 cm−1, 2928 cm−1 and 2856 cm−1. They are attributed to νsCH2(NH2), νasCH3/CH2 and νsCH3/CH2 vibration modes, respectively [63,66]. More precisely, the νsCH2(NH2) vibration is only visible on the SiHA-T spectrum (Fig. 4a) and the intensities of νasCH3/CH2 and $\nu_s CH_3/CH_2$ seem to decrease for SiHA-PEG and SiHA-BMP-2 (Fig. 4b and c). The second zoom is focused on the region of double-bonds (interval 1900–1400 cm^{-1}). A band at 1631 cm^{-1} attributed to the bending mode of water (δH2O) is visible on the spectrum of SiHA-T. The SiHA-PEG spectrum presents two bands at 1705 cm^{-1} and 1644 cm^{-1} attributed respectively to elongation of carbonyl in amide I (νC=O(-NH-R)) and amide II (νC=O(-NR_2)) functions [67], even if the contribution of δH2O cannot be excluded. Finally, the spectrum presents a shoulder at 1550 cm−1 attributed to the νC=C of the maleimide function. The intensity of these bands decreases on the SiHA-BMP-2 spectrum which also shows the bending mode of water (δH2O).

Table 1 shows the atomic composition of the surface of the spheres, determined by XPS survey analyses. In all cases, the Ca and P elements are visible. Their binding energies, determined from high-resolution XPS analyses, are regardless of the sample: 347.0 eV and 350.5 eV for Ca2p⅔ and Ca2p½, respectively; 132.8 eV and 133.8 eV for P2p⅔ and P2p½, respectively (Fig. 5) [68]. In comparison to ungrafted spheres analyses, the global percentages of nitrogen and carbon increase after the different steps of functionalization, evidencing the presence of the organic molecules (for SiHA, the presence of carbon is due to surface contamination by carbonaceous species). In the case of SiHA-BMP-2, the contribution of carbon is close to that of SiHA.

The O1s signal of unfunctionalized SiHA (Fig. 5) results from three contributions corresponding to physisorbed "H2O" (533.5 eV) [69,70], the phosphate groups "O-P" of the apatite structure (530.9 eV) and hydroxyl groups "OH" (532.2 eV) [71,72]. The latter contribution is due to the hydroxyl groups of the apatite structure and to those present at the ceramic surface. The "O-Si" contribution is combined with that of the "OH" group at 532.3 eV [71]. By analogy to O-Si-O bonds in silica [71,[73], [74], [75], [76], [77]], the Si2p peak, consisting in a single contribution at 102.0 eV, is attributed to the SiO4 tetrahedron in apatite (Fig. 5). After functionalisation, the Si2p XPS analysis displays only one wide peak (FWHM from 1.5 eV to 2.0 eV) attributed to two contributions: the alkoxysilane ("C-Si-O" [73,75]) and the SiHA substrate ("O-Si-O" [73,75]). Given the resolution of the spectrum, the peak decomposition would be meaningless and therefore the data is not shown.

For functionalized spheres, the C1s and N1s peaks are the sum of several contributions, the intensities of which vary regarding to the step of functionalization (Table 2). The spectra of SiHA-T spheres are characteristic of a carbon chain with a terminal amine function: "C-C/C-H" at 285.3 eV [73,78], "C-O" at 286.4 eV [73], "C-NH2" at 399.6 eV) [73,79] and its protonate form "C=NH3+" at 401.3 eV [69,73,79]. The slight contributions of C=O/N-C=O and O-C=O are due to unavoidable pollutions present on the sample surface. After the addition of NHS-PEG6-maleimide molecule, the contributions of 'C-O' (286.7 eV) and of "C=O/N-C=O" [80] increase and a new contribution is observed at 400.1 eV on N1s spectrum corresponding to "N-C=O" [69,81] (Fig. 6). The contribution at 401.6 eV relates to the protonate form of the amide function ("O=C-NH2+-" [82]). Indeed, the high binding energy component suggests a partial protonation of the amino group [83]. The N1s spectrum of SiHA-BMP-2 is similar to the one of SiHA-PEG except that the contribution of protonate nitrogen is lower ("C-NH_3+"). The spectrum presents also the contributions of "C=O/N-C=O" and "O-C=O" bonds at 287.9 eV and 289.3 eV, respectively.

The Fig. 7 presents the thermogravimetric analysis of SiHA and SiHA-T spheres and the mass emission curves of SiHA-T spheres. The plots can be divided in three domains: D1 from 30 to 300 °C, D2 from 300 to 650 °C and D3 above 650 °C. The Table 3 summarizes the molecular weights and the formulae which may be assigned to the organic fragments that are indexed on Fig. 7.

In the D1 domain (Fig. 7), the weight losses are low: 0.7% for unfunctionalized SiHA (red curve) and SiHA-T spheres (black curve), and 0.2% for SiHA-T control (blue curve). They are attributed to the release of adsorbed water and ethanol used as solvent (Tbp = 70 °C). Indeed, the following fragments are present (Fig. 7B): m/e = 16–18 due to water and m/e = 12, 43–45 and m/e = 46 (not represented on the graph because of its very weak intensity) due to ethanol.

The weight losses observed in D3 have an equivalent shape and a similar magnitude between the samples SiHA, SiHA-T and SiHA-T control (2.7%, 2.2% and 2.2%, respectively). This phenomenon corresponds on the mass curves of SiHA-T spheres (Fig. 7.B) to emission masses of m/e = 12, 13, 15 and 44 which may be attributed to CO2 and m/e = 16 and 17 due to OH.

The D2 domain [300–650 °C] shows a low weight loss for unfunctionalized SiHA spheres (0.7%). The curves of mass loss for SiHA-T and SiHA-T control are similar but in a four fold higher magnitude for SiHA-T than for its control (1.2% vs. 4.1%, respectively). This weight loss corresponds to the simultaneous emission of the following masses: m/e = 67 (-C2HOSi), 56–51 (amine and short siloxane chains), 42–37 (short carbonated chains containing or not silicon), 27–24 (short carbonated chains), 15 (-NH2/-CH3) and 12 for carbon (Fig. 7.B and Table 3). The emission mass m/e = 44 is the contribution of -C2H6N, SiO and CO2. The latter contribution is also visible on the mass curves of SiHA-T control (data not shown).

The mass curves of the SiHA-BMP-2 spheres present too weak intensities to be interpreted (data not shown), this is the reason why additional thermal analysis was performed on SiHA pellets functionalized with the same procedure as the one used for spheres.

The Fig. 8 presents the TG, dTG and MS analysis of SiHA-T and SiHA-BMP-2 pellets. In an equivalent manner, the weight losses recorded in the D1 domain (30 °C to 300 °C) for both samples are weak and attributed to adsorbed water (emission masses at m/e = 17 and 18).

In the D2 domain, as observed for the SiHA-T spheres, the emission masses at 12, 17, 18, 22, 30, 44 and 45 are intense. This contribution appears less intense for the SiHA-BMP-2 pellet and it is associated to a lower weight loss ($\Delta m = -0.25\%$ and -0.36% between 300 and 650 °C, respectively). Moreover, dTG plots show that the weight loss occurs in two steps with maxima at 380 °C and 550 °C for the Si-HA pellet. This was not clearly detectable on the TG plot of SiHA-T spheres (Fig. 7) because of the lower apparatus sensitivity. The first weight loss at 380 °C does not appear in the case of SiHA-BMP-2 but, in this a maximum of mass emissions at 12, 22, 44 and 45 is detected around 330 °C.

In the third domain (D3) of the thermogravimetric assays, two differences appear between SiHA-T and SiHA-BMP-2 pellets. The first one, which is clearly visible on the dTG of SiHA-BMP-2 (Fig. 8), is a weight loss between 800 °C and 900 °C with a maximum at 880 °C along with a shoulder around 810 °C. These mass losses are correlated to the emission mass m/e = 17, 18 and 44. The second one is observed between 620 °C and 780 °C and corresponds to a mass loss of 0.11% for SiHA-BMP-2, which has no equivalent in the plot of the SiHA-T pellet.

Biological activity of SiHA-BMP-2 spheres

The effective bioactivity of BMP-2 was assessed by culturing C3H10-BRE/Luc cells with grafted SiHA spheres for 24 h and measuring the activity of the expressed luciferase reporter gene. Their observation under an inverted microscope shows the presence of cells in contact with SiHA-BMP-2 spheres (Fig. 9.A). As expected, the luciferase activity increases in the presence of soluble BMP-2 (positive control) in a dose-dependent manner (Fig. 9.B). The bare spheres without BMP-2 (negative control) were not active whereas the luciferase activity of grafted BMP-2, for 2.5 mg and 5 mg spheres reached the same level of activity as soluble BMP-2 in the 30–50 ng/mL range.

Discussion:

Pure and monophasic SiHA spray-dried powder is composed of porous spheres. The absolute density being equivalent to the theoretical one, spheres contain few or no closed porosity and their relative density can be estimated to 92 ± 2% (since the surface porosity was estimated at 8 ± 2%). The open pores are broadly twice as long as they are wide and quite small with a Feret diameter ranging from 0.1 to 1.4 μm.

The thermal analyses show that at high temperature (Fig. 7 and Fig. 8, D3 domain), all the materials behave similarly with a weight loss associated to water and carbon dioxide release. This is due to decarbonation and deshydroxylation of SiHA ceramics which are more important for SiHA-BMP-2 because the grafting protocol uses aqueous solution (i.e. PBS).

At lower temperatures, even if a residual adsorption on SiHA-T materials cannot be excluded, the results obtained by XPS and TG/MS analyses show that the APTES is present and strongly bonded to the bioceramic surface. In the temperature domain D2, the emission of organic fragments between 300 and 650 °C (Fig. 7, Table 3) confirms the presence of the silane. Under Argon atmosphere, the liquid APTES (purity ≥98%) is fully evaporated at 250 °C with a maximum rate at 160 °C (data not shown). This evidences that a strong link exists between the silane and the ceramic, probably due to a covalent bond between the oxygen of the silane and the silicon and/or the phosphorus present in the apatite structure. Moreover, the silane is stabilized by the amine protonation which happens either in the case of covalently grafted molecules, via a reverse attachment of the terminal –NH2 to the surface [84], and also in the case of full chemisorption. Indeed, XPS analyses of nitrogen N1s peaks highlight two distinct contributions: "NH2" (Amine functions, 87%) and "NH3+" (13%). The slight "NH3+" contribution is due to the formation of hydrogen bonds with hydroxyl functions present on the surface [83] which are identified, on SiHA spheres, at 532.2 eV for hydroxyl groups "OH" and at 533.5 eV for adsorbed water "H2O". The presence of water is confirmed by the dehydration observed in the D1 domain on TG/MS analyses.

The only difference between the SiHA-T control and SiHA-T spheres (Fig. 7, D2 domain) is the presence of silane, the contribution of which may be estimated to 2.9%. The MS (Fig. 7) and dTG (Fig. 8) plots show two weight losses in the D2 domain which can be attributed to amine chains for the first one (maximum around 380 °C) and ethoxy chains for the second one (maximum around 550 °C). This can be explained by the energy of the Si-O bonds which is reported to vary from 370 to 540 kJ/mol [85,86] and therefore always expected to be higher than that of Si-C bonds (300–356 kJ/mol) [85,87].

Based on the assumption that 1.5 ethoxy functions of APTES are hydrolyzed [84], its "grafted" molar weight and the density of grafted molecules are estimated to be respectively 153.5 g/mol (for NH2(CH2)3Si(OCH2CH3)1.5) and 7.8 × 10−5 mol/m2 (i.e. 47 molecules/nm2). The silanisation was realized in a large excess of silane: 4 × 10−3 mol of silane (CAPTES = 0.2 mol/L, V = 20 mL) was introduced in the medium while the substrate had an area of 3.146 m2 (m = 1.3 g, SBET = 2.42 m2/g). This means that 1.27 × 10−3 mol of silane could potentially be bonded per square meter of powder. Thereby only a small quantity of silane reacts with the surface (around 6%). On the one hand, the density of potential P-OH and Si-OH graftable sites of the substrate can be estimated around 2.8 sites/nm2 [88] and the quantification by Ultraviolet-Visible (UV–Vis) photometric of primary amine sites of SiHA-T pellets [63] highlighted a density dNH2 of 7.0 × 10−6 ± 0.5 × 10−6 mol/m2 (4.2 sites/nm2). On the other hand, although the XPS analyzed area is large (300 × 700 μm2 with a depth around 5 nm), calcium and phosphorus elements are still visible whatever the substrates. So, this data is consistent with a partial coverage of the surface by small heaps of APTES molecules presenting few free amine functions on their top [84].

The addition of NHS-PEG6-maleimide and thiolated rh-BMP-2 to the surface is highlighted by the modification of the nitrogen and carbon contributions on XPS analyses. Indeed for SiHA-T, the carbon peak is mostly due to "C-C/C-H" and the one of nitrogen to the amine function 'NH2'. After the addition of NHS-PEG6-maleimide the contribution of "C-O/C-N" increases and the contribution of "N-C=O" appears [69,81] (Fig. 6). Moreover, the contribution of "NH2" is shifted from 399.6 to 400.1 eV attesting the presence of amide functions (N-C=O/O=C-N-C=O). These evolutions are due to the presence of the maleimide function (O=C-N-C=O) and to the amide (NH-C=O) coming from the reaction of the NHS function with the amine of silane. The same observation and conclusion can be done after the addition of thiolated rh-BMP-2. In the latter case, the contributions of "N-C=O/O=C-N-C=O" and "O-C=O" are more important because of the peptide bonds.

Concerning the TG/MS analyses for SiHA-BMP-2 in the D2 domain (Fig. 8), the first weight loss contribution noticed at 380 °C for SiHA-T is not observed because of the absence of the amine chain related to the grafting of NHS-PEG6-maleimide and then thiolated rh-BMP-2 molecules. The second maximum at 550 °C, attributed to unhydrolyzed ethoxy functions, is still present. The new mass emissions around 330 °C may be assigned to the breaking of the side-chain of amino-acids constituting the BMP-2 proteins. The new weight loss in the beginning of the third domain of temperature (0.11% between 620 °C and 780 °C) corresponds to the detachment of the whole grafted molecules (APTES + NHS-PEG6-maleimide + thiolated rh-BMP-2, see Fig. 1). The fact that no associated mass emission is observed may be explained by both the low quantity of the grafted molecules (around 4 × 10−8 mol/g of SiHA pellets) and the possible condensation of these heavy molecules in the apparatus.

The biological evaluation attests the activity of the grafted spheres. Interestingly, the luciferase activity from C3H10-BRE/Luc cells significantly increases in the presence of increasing amounts of SiHA-BMP-2 spheres (Fig. 9B). The fact that the bare spheres without any grafted BMP-2 adsorbed on it were not active confirms that the BMP-2 grafted onto spheres is the only agent promoting the BRE-Luc expression activation. These results provide evidence that the BMP-2 grafted onto SiHA spheres has remained bioactive.

Conclusion

Calibrated spheres made of SiHA ceramics have been successfully shaped by spray-drying and functionalized by covalent immobilization of bone morphogenetic protein-2 (BMP-2). The grafting protocol enables low surface densities of proteins to be obtained. The *in vitro* evaluations conducted with C3H10 cell line (C3H10-BRE/Luc cells) have shown that the BMP-2 proteins are still bioactive. Further *in vivo* investigations are under progress to confirm the activity of BMP-2 proteins and to validate its controlled release.

Acknowledgments

The authors thank the French Agence Nationale de la Recherche in the scope of the LabEx SigmaLim (ANR-10-LABX-0074-01) and the “CeramOs” project (ANR-13-BSV5-0002) for the funding of this study. The authors are grateful to Etienne Laborde for assistance in XPS analyses and Solange Degot for TG/MS experiments. Disclosure Statement

References

[1] R. Heary, R. Schlenk, T. Sacchieri, D. Barone, C. Brotea, R. Fessler, V. Sonntag, J. Ratliff, P. Cooper, M. Kaiser, P. McCormick, Persistent iliac crest donor site pain: independent outcome assessment, Neurosurgery 50 (3) (2002) 510–517.

[2] M. Hinsenkamp, Muylle Lc, T. Eastlund, D. Fehily, L. Noel, D. Strong, Adverse reactions and events related to musculoskeletal allografts: reviewed by the World Health Organisation Project NOTIFY, Int. Orthop. 36 (3) (2012) 633–641.

[3] L.L. Hench, J.M. Polak, Third-generation biomedical materials, Science 295 (5557) (2002) 1014–1017.

[4] M. Jarcho, Calcium phosphate ceramics as hard tissue prosthetics, Clin. Orthop. Relat. Res. (157) (1981) 259–278.

[5] J. Elliott, Structure and chemistry of the apatites and other calcium orthophosphates, Studies in Inorganic Chemistry, Elsevier Amsterdam edition, Vol. 18 Elsevier Eds., Amsterdam, 1994.

[6] S. Bose, M. Roy, A. Bandyopadhyay, Recent advances in bone tissue engineering scaffolds, Trends Biotechnol. 30 (10) (2012) 546–554.

[7] D. Tadic, M. Epple, A thorough physicochemical characterisation of 14 calcium phosphate-based bone substitution materials in comparison to natural bone, Biomaterials 25 (6) (2004) 987–994.

[8] Saikia Kb, T. Bhattacharya, S. Bhuyan, D. Talukdar, S. Saikia, P. Jitesh, Calcium phosphate ceramics as bone graft substitutes in filling bone tumor defects, Indian J. Orthop. 42 (2) (2008) 169–172.

[9] W. Habraken, P. Habibovic, M. Epple, M. Bohner, Calcium phosphates in biomedical applications: materials for the future? Mater. Today 19 (2) (2016) 69–87.

[10] H. Petite, V. Viateau, W. Bensaid, A. Meunier, C. de Pollak, M. Bourguignon, K. Oudina, L. Sedel, G. Guillemin, Tissue-engineered bone regeneration, Nat. Biotechnol. 18 (9) (2000) 959–963.

[11] M. Lind, Growth factor stimulation of bone healing, Acta Orthop. Scand. 69 (sup283) (1998) 1–37.

[12] S. Oh, N. Oh, M. Appleford, J.L. Ong, Bioceramics for tissue engineering applications-a review, Am. J. Biochem. Biotechnol. 2 (2) (2006) 49–56.

[13] A. Ratcliffe, Difficulties in the translation of functionalized biomaterials into regenerative medicine clinical products, Biomaterials 32 (18) (2011) 4215–4217.

[14] R. Dimitriou, E. Tsiridis, P.V. Giannoudis, Current concepts of molecular aspects of bone healing, Injury 36 (12) (2005) 1392–1404.

[15] K. Tsuji, A. Bandyopadhyay, B. Harfe, K. Cox, S. Kakar, L. Gerstenfeld, T. Einhorn, C. Tabin, V. Rosen, BMP2 activity, although dispensable for bone formation, is required for the initiation of fracture healing, Nat. Genet. 38 (12) (2006) 1424–1429.

[16] L. Bonassar, C.A. Vacanti, Tissue engineering: the first decade and beyond, J. Cell. Biochem. Suppl. 30-31 (1998) 297–3003.

[17] J. Kim, T. Ma, Bioreactor strategy in bone tissue engineering: pre-culture and osteogenic differentiation under two flow configurations, Tissue Eng. A 18 (21−22) (2012) 2354–2364.

[18] S.D. Boden, T.A. Zdeblick, H.S. Sandhu, S.E. Heim, The use of rhBMP-2 in interbody fusion cages: definitive evidence of osteoinduction in humans: a preliminary report, Spine 25 (3) (2000) 376–381.

[19] H. Inoda, G. Yamamoto, T. Hattori, Histological investigation of osteoinductive properties of rh-BMP2 in a rat calvarial bone defect model, J. Cranio-Maxillofac. Surg. 32 (6) (2004) 365–369.

[20] J. Boerckel, B. Uhrig, N. Willett, N. Huebsch, R. Guldberg, Mechanical regulation of vascular growth and tissue regeneration in vivo, Proc. Natl. Acad. Sci. U. S. A. 108 (37) (2011) E674–E680.

[21] G. Finkenzeller, S. Hager, G. Stark, Effects of bone morphogenetic protein 2 on human umbilical vein endothelial cells, Microvasc. Res. 84 (1) (2012) 81–85.

[22] L.B.E. Shields, G.H. Raque, S.D. Glassman, M. Campbell, T. Vitaz, J. Harpring, C.B. Shields, Adverse effects associated with high-dose recombinant human bone morphogenetic protein-2 use in anterior cervical spine fusion, Spine 31 (5) (2006) 542–547.

[23] L.Y. Carreon, S.D. Glassman, D.C. Brock, J.R. Dimar, R.M. Puno, M.J. Campbell, Adverse events in patients re-exposed to bone morphogenetic protein for spine surgery, Spine 33 (4) (2008) 391–393.

[24] E. Vaccaro, Controversies in Spine Surgery: Best Evidence Recommendations, Thieme Eds., (2010).

[25] K. Lee, C. Taghavi, K. Song, C. Sintuu, J. Yoo, G. Keorochana, S. Tzeng, Z. Fei, J. Liao, J. Wang, Inflammatory characteristics of rhBMP-2 in vitro and in an in vivo rodent model, Spine 36 (3) (2011) 149–154.

[26] E. Carragee, E. Hurwitz, B. Weiner, A critical review of recombinant human bone morphogenetic protein-2 trials in spinal surgery: emerging safety concerns and lessons learned, Spine J. 11 (6) (2011) 471–491.

[27] L. Andersson, K.E. Kahnberg, M.A. Pogrel, Oral and maxillofacial surgery, WileyBlackwell, United Kingdom, Chichester, West Sussex, 2010.

[28] M.A. Lauzon, Marcos B. Bergeron b, N. Faucheux, Bone repair: new developments in growth factor delivery systems and their mathematical modeling, J. Control. Release 162 (3) (2012) 502–520.

[29] M. Chatzinikolaidou, T. Lichtinger, R. Muller, H. Jennissen, Peri-implant reactivity and osteoinductive potential of immobilized rhBMP-2 on titanium carriers, Acta Biomater. 6 (11) (2010) 4405–4421.

[30] A.E. Mercado, J. Ma, X. He, E. Jabbari, Release characteristics and osteogenic activity of recombinant human bone morphogenetic

protein-2 grafted to novel self-assembled poly(lactide-co-glycolide fumarate) nanoparticles, J. Control. Release 140 (2) (2009) 148–156.

[31] S. Vukicevic, K.T. Sampath, Bone Morphogenic Proteins: Regeneration of Bone and beyond, Birkhauser Eds., (2004).

[32] M. D'Este, D. Eglin, Hydrogels in calcium phosphate moldable and injectable bone substitutes: sticky excipients or advanced 3-D carriers? Acta Biomater. 9 (3) (2013) 5421–5430.

[33] Rakic M. Struillou Xb, Zb Badran, Lb Macquigneau, C. Colombeix, P. Pilet, C. Verner, O. Gauthier, P. Weiss, Ab Soueidan, The association of hydrogel and biphasic calcium phosphate in the treatment of dehiscence-type peri-implant defects: an experimental study in dogs, J. Mater. Sci. Mater. Med. 24 (12) (2013) 2749–2760.

[34] S.H. Jeong, Y.H. Koh, S.W. Kim, J.U. Park, H.E. Kim, J.E. Song, Strong and biostable hyaluronic acid-calcium phosphate nanocomposite hydrogel via in situ precipitation process, Biomacromolecules 17 (3) (2016) 841–851.

[35] J.P. Chen, M.J. Tsai, H.T. Liao, Incorporation of biphasic calcium phosphate microparticles in injectable thermoresponsive hydrogel modulates bone cell proliferation and differentiation, Colloids Surf. B: Biointerfaces 110 (2013) 120–129.

[36] E.M. Carlisle, Silicon: a possible factor in bone calcification, Science 167 (3916) (1970) 279–280.

[37] K. Schwarz, D. Milne, Growth-promoting effects of silicon in rats, Nature 239 (5371) (1972) 333–334.

[38] F.H. Nielsen, R. Poellot, Dietary silicon affects bone turnover differently in ovariectomized and sham-operated growing rats, J. Trace Elem. Exp. Med. 17 (3) (2004) 137–149.

[39] J. Damen, J. Ten Cate, Silica-induced precipitation of calcium phosphate in the presence of inhibitors of hydroxyapatite formation, J. Dent. Res. 71 (3) (1992) 453–457.

[40] Jugdaohsingh Rbc, Silicon and bone health, J. Nutr. Health Aging 11 (2) (2007) 99–110.

[41] D.M. Reffitt, N. Ogston, R. Jugdaohsingh, H.F.J. Cheung, B.A.J. Evans, R.P.H. Thompson, J.J. Powell, G.N. Hampson, Orthosilicic acid stimulates collagen type I synthesis and osteoblastic differentiation in human osteoblast-like cells in vitro, Bone 32 (2) (2003) 127–135.

[42] J. Henstock, L. Canham, S. Anderson, Silicon: the evolution of its use in biomaterials, Acta Biomater. 11 (2015) 17–26.

[43] E. Boanini, M. Gazzano, A. Bigi, Ionic substitutions in calcium phosphates synthesized at low temperature, Acta Biomater. 6 (6) (2010) 1882–1894.

[44] M. Bohner, Silicon-substituted calcium phosphates - a critical view, Biomaterials 30 (32) (2009) 6403–6406.

[45] J.H. Shepherd, S.M. Best, Calcium phosphate scaffolds for bone repair, J. Miner. Met. Mater. Soc. 63 (4) (2011) 83–92.

[46] V. Nagineni, A. James, M. Alimi, C. Hofstetter, B. Shin, I. Njoku, A. Tsiouris, R. Härtl, Silicate-substituted calcium phosphate ceramic bone graft replacement for spinal fusion procedures, Spine 37 (20) (2012) E1264–E1272.

[47] D. Fredericks, E. Petersen, N. Sahai, K. Corley, N. De Vries, N. Grosland, J. Smucker, Evaluation of a novel silicate substituted hydroxyapatite bone graft substitute in a rabbit posterolateral fusion model, Iowa Orthop. J. 33 (2013) 25–32.

[48] I.R. Gibson, S.M. Best, W. Bonfield, Chemical characterization of silicon-substituted hydroxyapatite, J. Biomed. Mater. Res. 44 (4) (1999) 422–428.

[49] H. Kim, Ceramic bioactivity and related biometric strategy, Solid State Mater. Sci. 7 (2003) 289–299.

[50] M. Palard, E. Champion, S. Foucaud, Synthesis of silicated hydroxyapatite Ca10(PO4)6−x(SiO4)x(OH)2−x, J. Solid State Chem. 181 (8) (2008) 1950–1960.

[51] M. Palard, J. Combes, E. Champion, S. Foucaud, A. Rattner, D. Bernache-Assollant, Effect of silicon content on the sintering and biological behaviour of Ca10(PO4)6−x(SiO4)x(OH)2−x ceramics, Acta Biomater. 5 (4) (2009) 1223–1232.

[52] D. Marchat, M. Zymelka, C. Coelho, L. Gremillard, L. Joly-Pottuz, F. Babonneau, C. Esnouf, J. Chevalier, D. Bernache-Assollant, Accurate characterization of pure silicon-substituted hydroxyapatites powders synthesized by a new precipitation route, Acta Biomater. 9 (2012) 6992–7004.

[53] T. Furuzono, K. Sonoda, J. Tanaka, A hydroxyapatite coating covalently linked onto a silicone implant material, J. Biomed. Mater. Res. 56 (2001) 9–16.

[54] S. Kalinina, H. Gliemann, M. Lopez-Garcia, A. Petershans, J. Auernheimer, T. Schimmel, M. Bruns, A. Schambony, H. Kessler, D. Wedlich, Isothiocyanatefunctionalized RGD peptides for tailoring cell-adhesive surface patterns, Biomaterials 29 (20) (2008) 3004–3013.

[55] R. Detsch, I. Dieser, U. Deisinger, F. Uhl, S. Hamisch, G. Ziegler, G. Lipps, Biofunctionalization of dispense-plotted hydroxyapatite scaffolds with peptides: quantification and cellular response, J. Biomed. Mater. Res. A 92 (2) (2010) 493–503.

[56] M.C. Durrieu, S. Pallu, F. Guillemot, R. Bareille, J. Amedee, C. Baquey, C. Labrugere, M. Dard, Grafting RGD containing peptides onto hydroxyapatite to promote osteoblastic cells adhesion, J. Mater. Sci. Mater. Med. V15 (7) (2004) 779–786.

[57] G. Balasundaram, M. Sato, T.J. Webster, Using hydroxyapatite nanoparticles and decreased crystallinity to promote osteoblast adhesion similar to functionalizing with RGD, Biomaterials 27 (14) (2006) 2798–2805.

[58] A. Schuessele, H. Mayr, J. Tessmar, A. Goepferich, Enhanced bone morphogenetic protein-2 performance on hydroxyapatite ceramic surfaces, J. Biomed. Mater. Res. A 90((4) (2009) 959–971.

[59] P. Schaffner, J. Meyer, M. Dard, B. Nies, S. Verrier, H. Kessler, M. Kantlehner, Induced tissue integration of bone implants by coating with bone selective RGDpeptides in vitro and in vivo studies, J. Mater. Sci. Mater. Med. 10 (1999) 837–839.

[60] M. Kantlehner, P. Schaffner, D. Finsinger, J. Meyer, A. Jonczyk, B. Diefenbach, B. Nies, G. Holzemann, S.L. Goodman, H. Kessler, Surface coating with cyclic RGD peptides stimulates osteoblast adhesion and proliferation as well as bone formation, Eur. J. Clin. Chem. Clin. Biochem. 1 (2) (2000) 107–114.

[61] Liu Zb, S. Tabakman, Z. Chen, H. Dai, Preparation of carbon nanotube bioconjugates for biomedical applications, Nat. Protoc. 4 (9) (2009) 1372–1382.

[62] J. Klaehn, T. Luther, C. Orme, M. Jones, A. Wertsching, E. Peterson, Soluble Nsubstituted organosilane polybenzimidazoles, Macromolecules 40 (2007) 7487–7492.

[63] E. Poli, V. Chaleix, C. Damia, Z. Hjezi, E. Champion, V. Sol, Efficient quantification of primary amine functions grafted onto apatite ceramics by using two UV-Vis spectrophotometric methods, Anal. Methods 6 (2014) 9622–9627.

[64] C. Rey, B. Collins, T. Goehl, I.R. Dickson, M.J. Glimcher, The carbonate environment in bone mineral: a resolution-enhanced fourier transform infrared spectroscopy study, Calcif. Tissue Int. 45 (3) (1989) 157–164.

[65] D. Logeart-Avramoglou, M. Bourguignon, K. Oudina, P. Ten Dijke, H. Petite, An assay for the determination of biologically active bone morphogenetic proteins using cells transfected with an inhibitor of differentiation promoter-luciferase construct, Anal. Biochem. 349 (1) (2006) 78–86.

[66] V.K.S. Hsiao, J.R. Waldeisen, Y. Zheng, P.F. Lloyd, T.J. Bunning, T.J. Huang, Aminopropyltriethoxysilane (APTES)-functionalized nanoporous polymeric gratings: fabrication and application in biosensing, J. Mater. Chem. 17 (2007) 4896–4901.

[67] R.M. Silverstein, F.X. Webster, D.J. Kiemle, D.L. Bryce, Spectrometric Identification of Organic Compounds, 8th edition, Wiley & Sons Eds., 2014.

[68] A. Boyd, G. Burke, H. Duffy, M. Holmberg, C. O'Kane, B. Meenan, P. Kingshott, Sputter deposited bioceramic coatings: surface characterisation and initial protein adsorption studies using surface-MALDI-MS, J. Mater. Sci. Mater. Med. 22 (1) (2011) 71–84.

[69] G. Iucci, M. Dettin, C. Battocchio, R. Gambaretto, C. Di Bello, G. Polzonetti, Novel immobilizations of an adhesion peptide on the TiO2 surface: an XPS investigation, Mater. Sci. Eng. C 27 (2007) 1201–1206.

[70] Y. Song, H. Hildebrand, P. Schmuki, Optimized monolayer grafting of 3-aminopropyltriethoxysilane onto amorphous, anatase and rutile TiO2, Surf. Sci. 604 (2010) 346–353.

[71] Balas F, Perez-Pariente J and Vallet-Regi M. In vitro bioactivity of silicon-substituted hydroxyapatites. J. Biomed. Mater. Res. A 66A:364–375, 2003.

[72] C. Yang, K. Cheng, W. Weng, C. Yang, Immobilization of RGD peptide on HA coating through a chemical bonding approach, J. Mater. Sci. Mater. Med. 20 (2009) 2349–2352.

[73] D. Briggs, Surface Analysis by Auger and X-ray Photoelectron Spectroscopy, IM Publications, 2003.

[74] J. Perez-Pariente, F. Balas, M. Vallet-Regi, Surface and chemical study of SiO2-P2O5CaO-(MgO) bioactive glasses, Chem. Mater. 12 (3) (2000) 750–755.

[75] Y. Hijikata, H. Yaguchi, M. Yoshikawa, S. Yoshida, Composition analysis of SiO2/ SiC interfaces by electron spectroscopic measurements using slope-shaped oxide films, Appl. Surf. Sci. 184 (1–4) (2001) 161–166.

[76] G. Beshkov, V. Krastev, K. Grigorov, H. Maciel, T.A. Tang, V. Huang, X-ray photoelectron spectroscopy study of phosphorus silicate glasses, Surf. Coat. Technol. 161 (1) (2002) 11–19.

[77] V. Aaritalo, S. Areva, M. Jokinen, M. Linden, T. Peltola, Sol-gel-derived TiO2-SiO2 implant coatings for direct tissue attachment. Part I: design, preparation and characterization, J. Mater. Sci. Mater. Med. 18 (9) (2007) 1863–1873.

[78] J. Xu, K. Khor, Chemical analysis of silica doped hydroxyapatite biomaterials consolidated by a spark plasma sintering method, J. Inorg. Biochem. 101 (2) (2007) 187–195.

[79] M. Seach, D. Briggs, Practical Surface Analysis, (1990).

[80] I. Bilem, P. Chevallier, L. Plawinski, E. Sone, M. Durrieu, G. Laroche, RGD and BMP2 mimetic peptide crosstalk enhances osteogenic commitment of human bone marrow stem cells, Acta Biomater. 36 (2016) 132–142.

[81] X. Liu, B. Yu, Q. Huang, R. Liu, Q. Feng, Q. Cai, S. Mi, In vitro BMP-2 peptide release from thiolated chitosan based hydrogel, Int. J. Biol. Macromol. 93 (Part A) (2016) 314–321.

[82] J. Moulder, W. Stickle, P. Sobol, K. Bomben, Handbook of X-ray Photoelectron Spectroscopy, Physical Electronics Inc., 1996.

[83] J. Bohmler, L. Ploux, V. Ball, K. Anselme, A. Ponche, Necessity of a thorough characterization of functionalized silicon wafers before biointerface studies, J. Phys. Chem. C 115 (22) (2011) 11102–11111.

[84] M. Zhu, M. Lerum, W. Chen, How to prepare reproducible, homogeneous, and hydrolytically stable aminosilane-derived layers on silica, Langmuir 28 (1) (2012) 416–423.

[85] Y. El Kortobi, J. de la D'espinose Caillerie, A. Legrand, Local composition of silicon oxycarbides obtained by laser spray pyrolysis, Chem. Mater. 9 (1997) 632–639.

[86] L. Byczynski, M. Dutkiewicz, H. Maciejewski, Thermal degradation studies of poly (urethane-siloxane) thermosets based on co-poly(dimethyl)(methyl, hydroxypolyoxyethylenepropyl) siloxane, Thermochim. Acta 589 (2014) 252–261.

[87] M. Kim, J. Lee, Characterization of amorphous SiC:H films deposited from hexamethyldisilazane, Thin Solid Films 303 (1997) 173–179.

[88] W. Neuman, M. Neuman, The nature of the mineral phase of bone, Chem. Rev. 53 (1) (1953) 1–45.Corresponding author:

Corresponding author:
C. Damia ; E-mail: chantal.damia@unilim.fr

Received 22 January 2017,
Revised 18 September 2017,
Accepted 28 January 2018,
Available online 31 January 2018

How to cite this article: Chantal Damia, David Marchat, Charly Lemoine, Nathalie Douard, Vincent Chaleix, Vincent Sol, Nathanaël Larochette, Delphine Logeart-Avramoglou, Joël Brie, Eric Champion, Functionalization of phosphocalcic bioceramics for bone repair applications, Materials Science and Engineering: C, Vol 95, 2019, Pages 343-354, https://doi.org/10.1016/j.msec.2018.01.008.

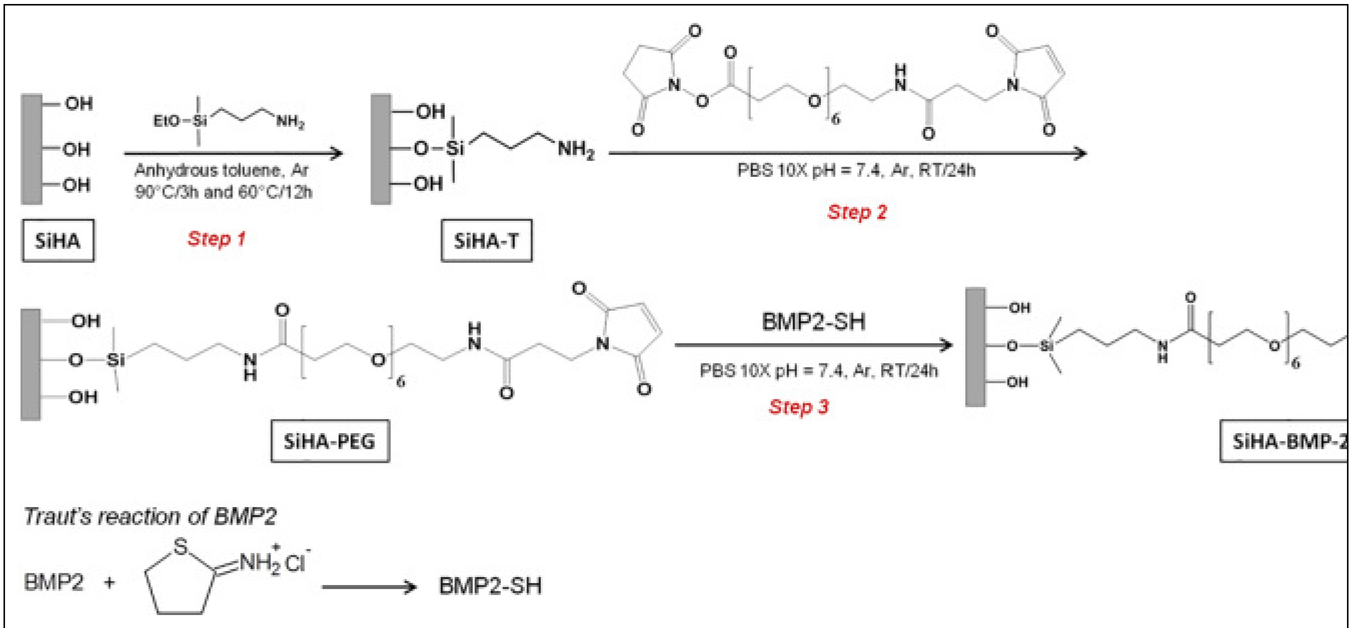

Figure 1: Surface modification of SiHA spheres with BMP-2 using a grafting-from approach.

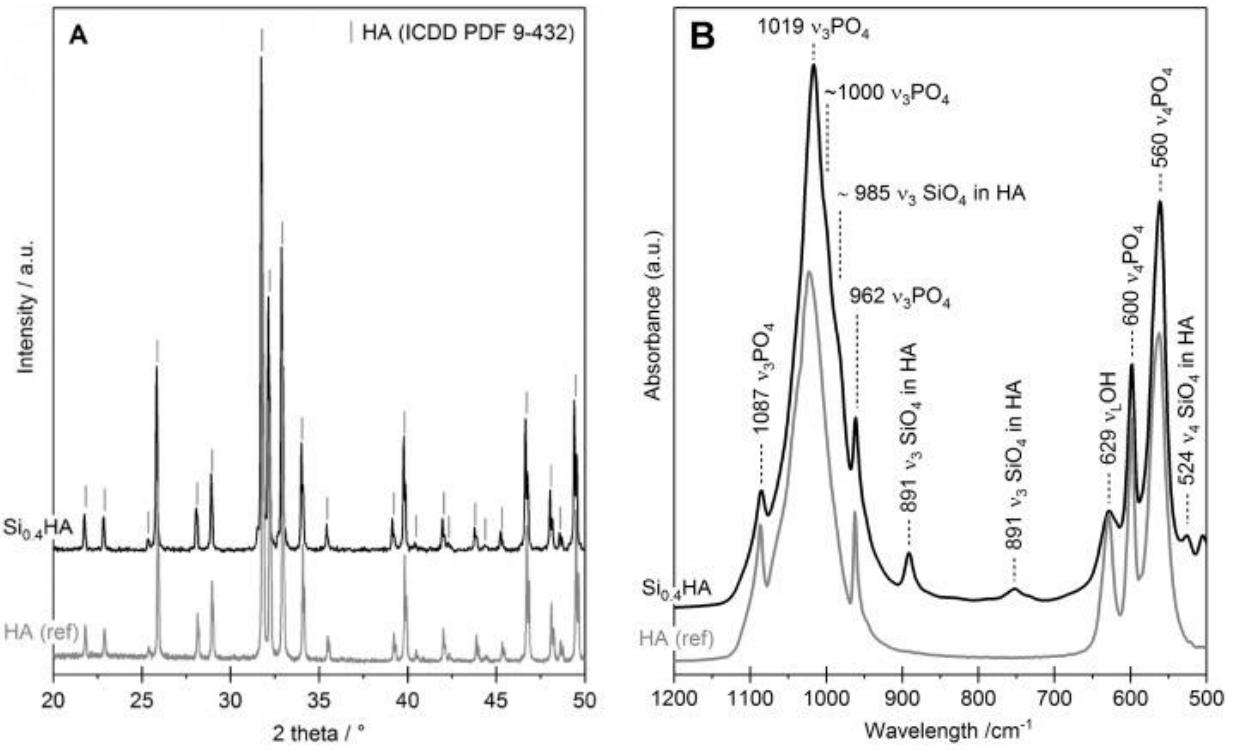

Figure 2: (A) XRD patterns and (B) FTIR spectra of grinded SiHA spheres and HA powder sintered at 1140 °C for 1 h under steam (pH2O = 286 mbar). HA powder has been synthesized according to D. Marchat et al. [52].

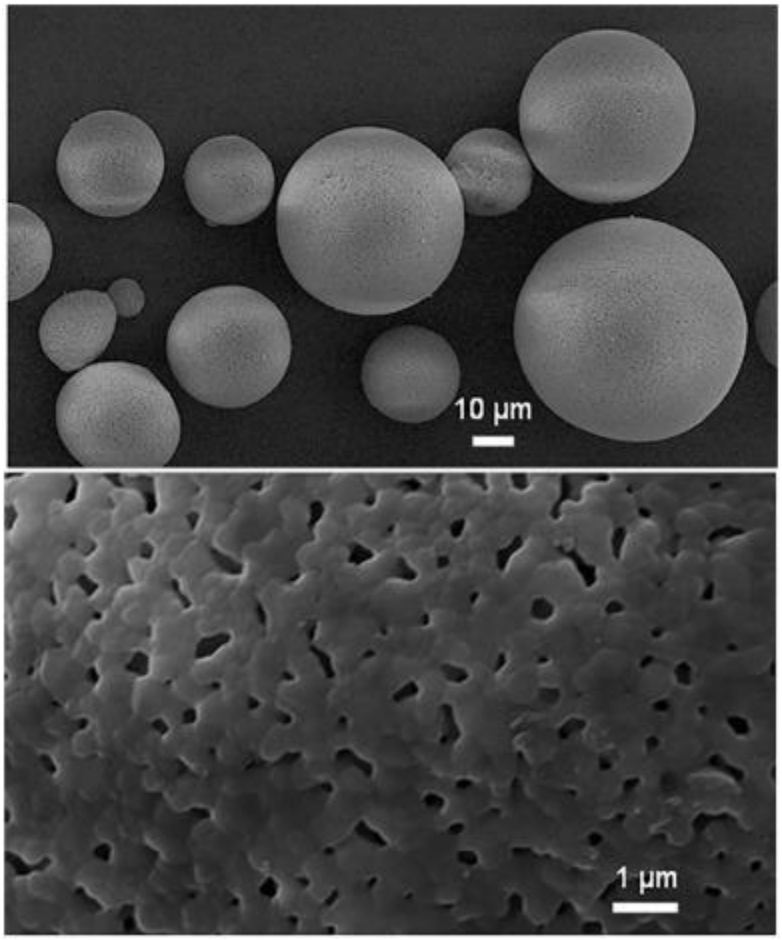

Figure 3: SEM micrographs of the SiHA spheres sintered at 1140 °C for 1 h under steam (pH20 = 286 mbar).

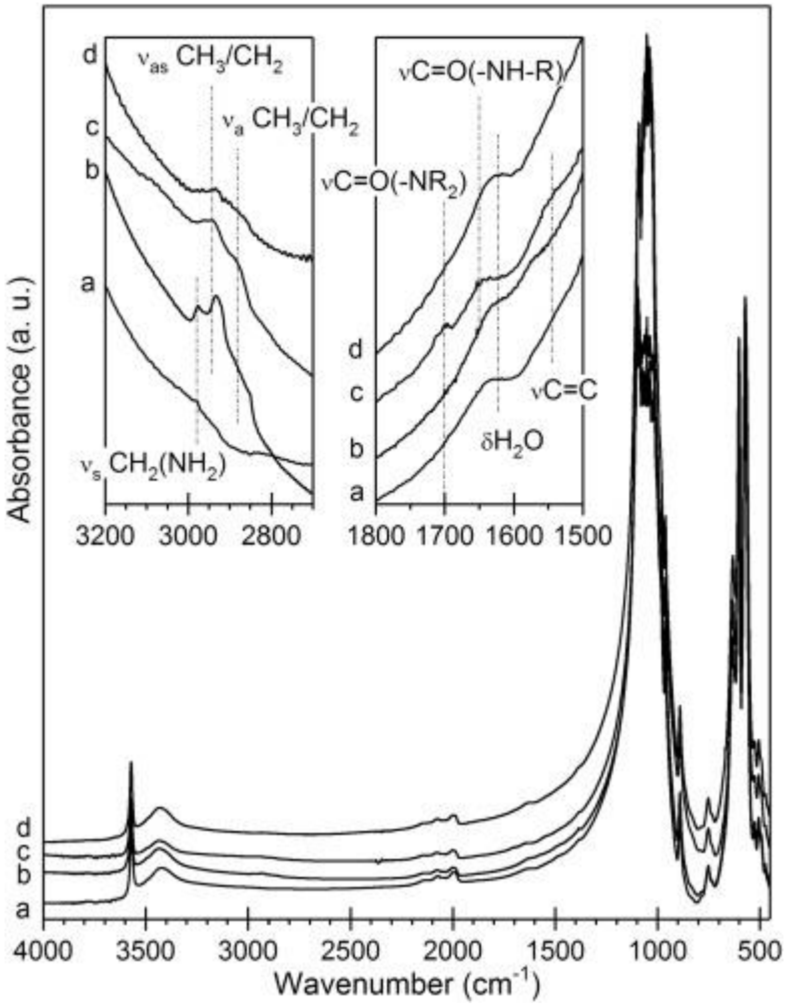

Figure 4: FTIR spectra of unfunctionalised and functionalized SiHA spheres: (a) SiHA, (b) SiHA-T, (c) SiHA-PEG and (d) SiHA-BMP-2. The spectra are saturated in absorbance because of the acquisition conditions required to highlight organic species vibrations (2.8 w/w in KBr).

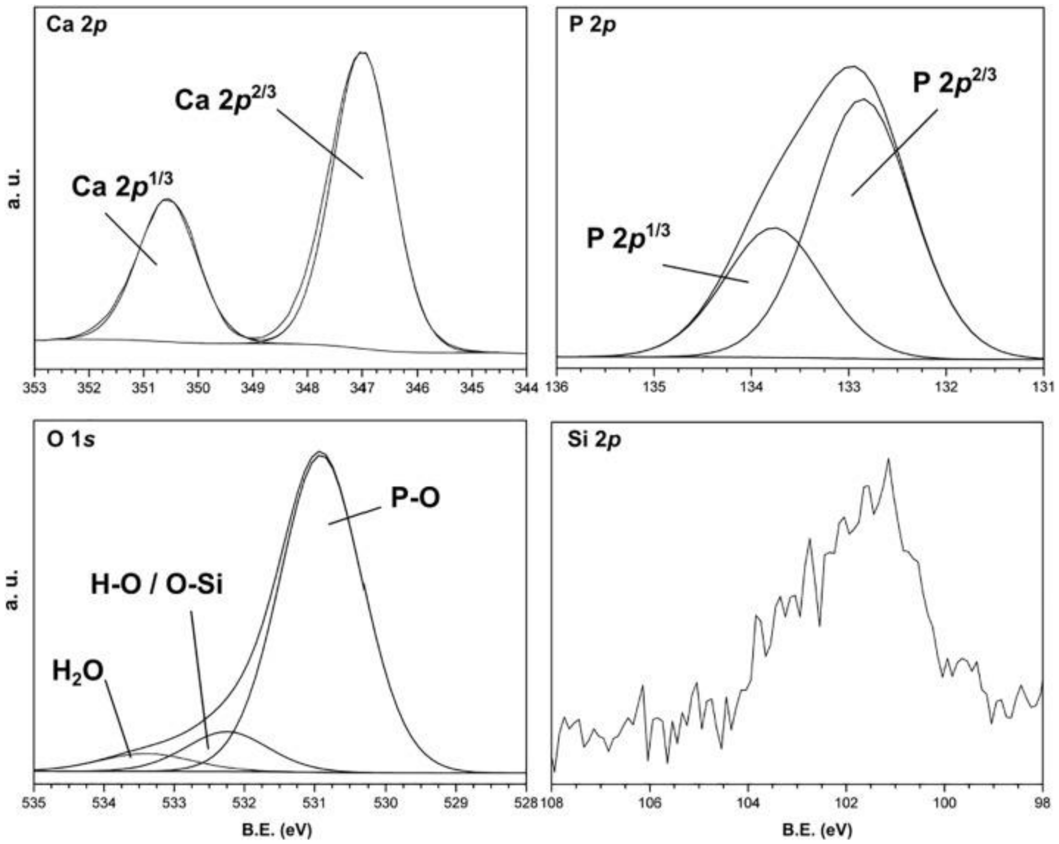

Figure 5: Spectra of the XPS high-resolution analysis of Ca2*p*, P2*p*, O1*s* and Si2*p* for SiHA spheres. The spectra of calcium, phosphorus and silicon are also representative of those of all the functionalized samples.

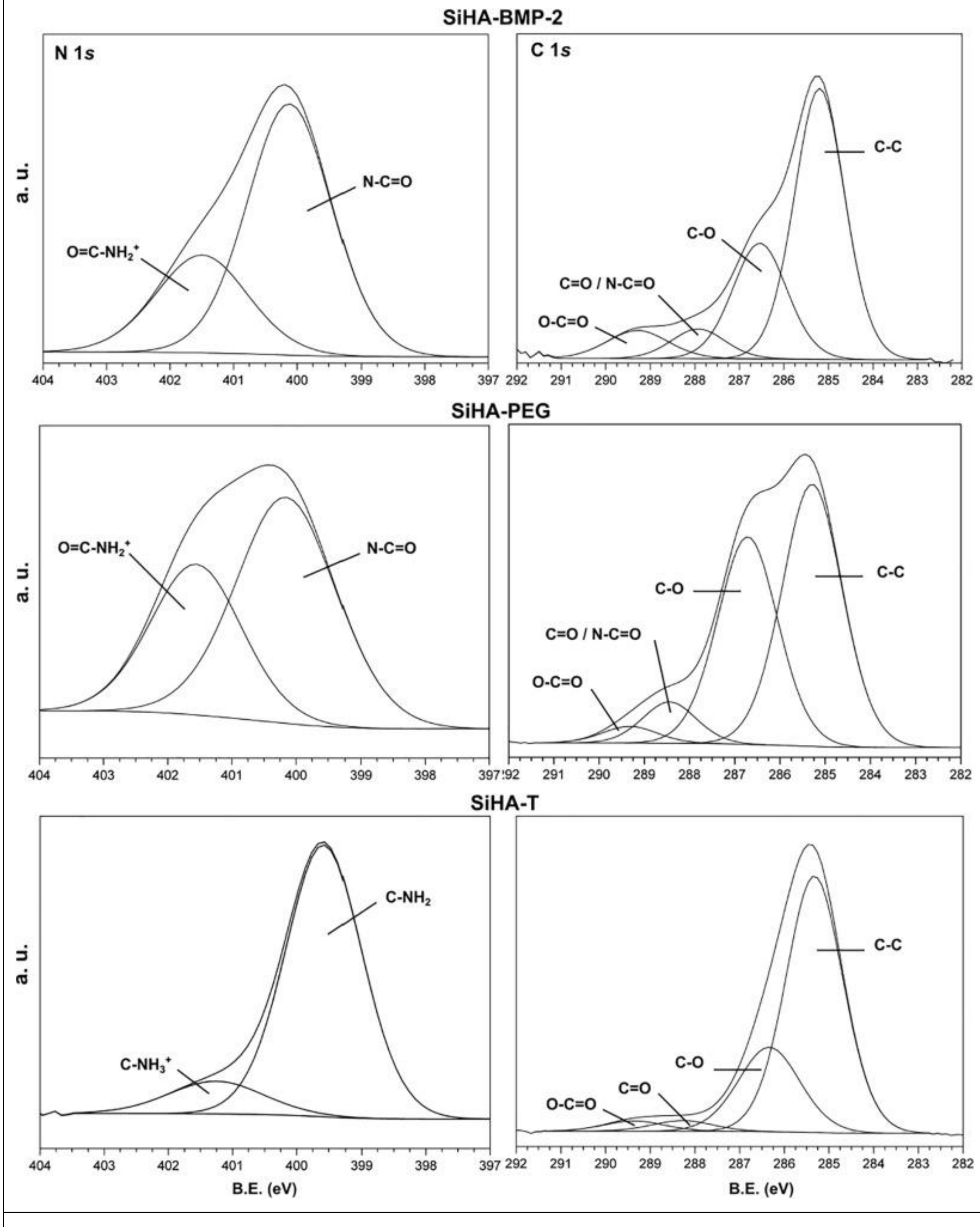

Figure 6: Spectra of the XPS high-resolution analysis of (left) N1*s* and (right) C1*s* for SiHA-T, SiHA-PEG and SiHA-BMP-2 spheres.

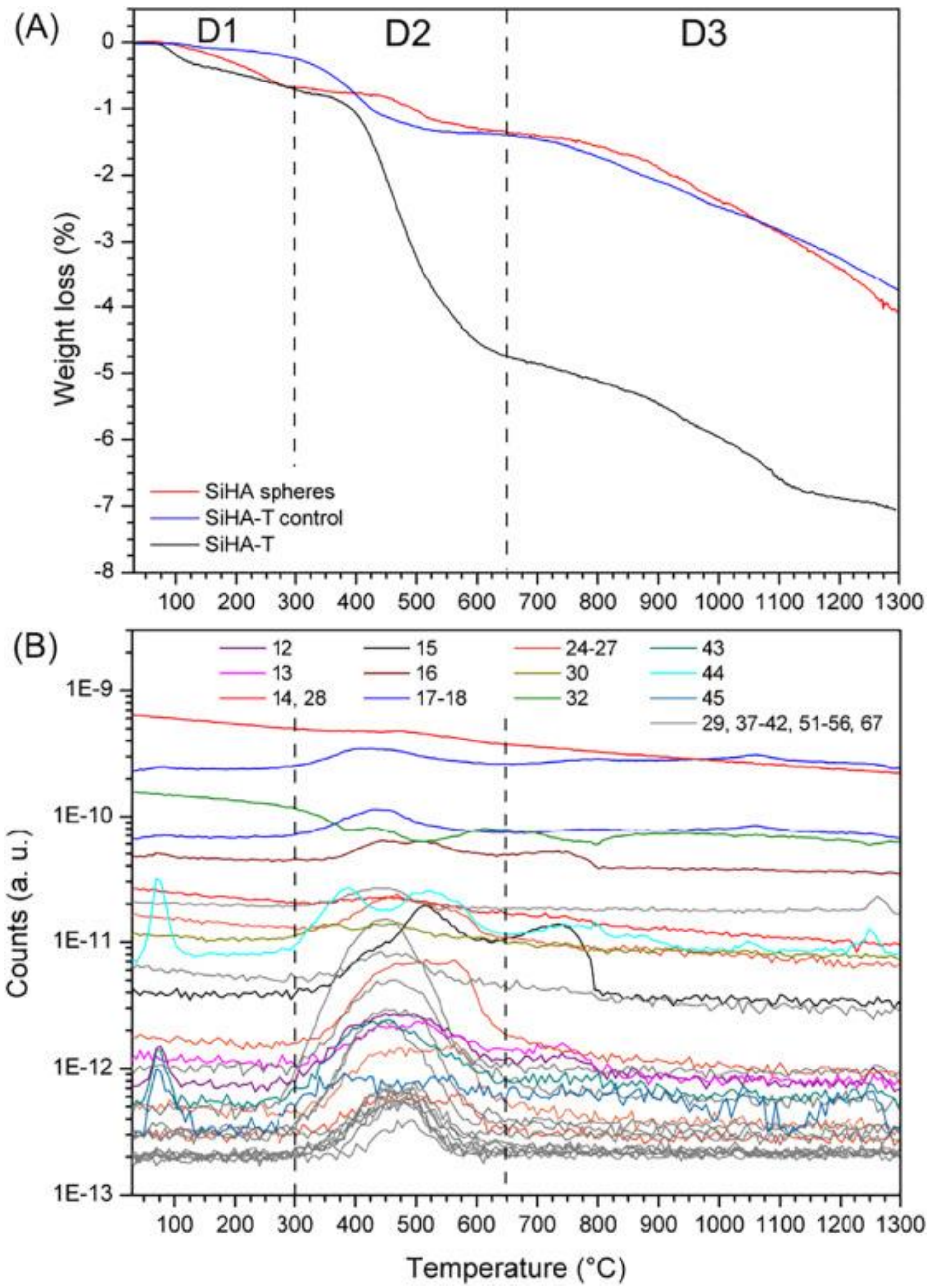

Figure 7: (A) Thermogravimetry (TG) of (red curve) unfunctionalized SiHA, (blue curve) SiHA-T control (*i.e.* spheres having followed the grafting protocol but without T molecules) and (black curve) SiHA-T spheres. (B) Mass emission curves of SiHA-T spheres. The m/e values are indicated on the top of the graph. To simplify the lecture, the curves having the same profiles are represented with the same color.

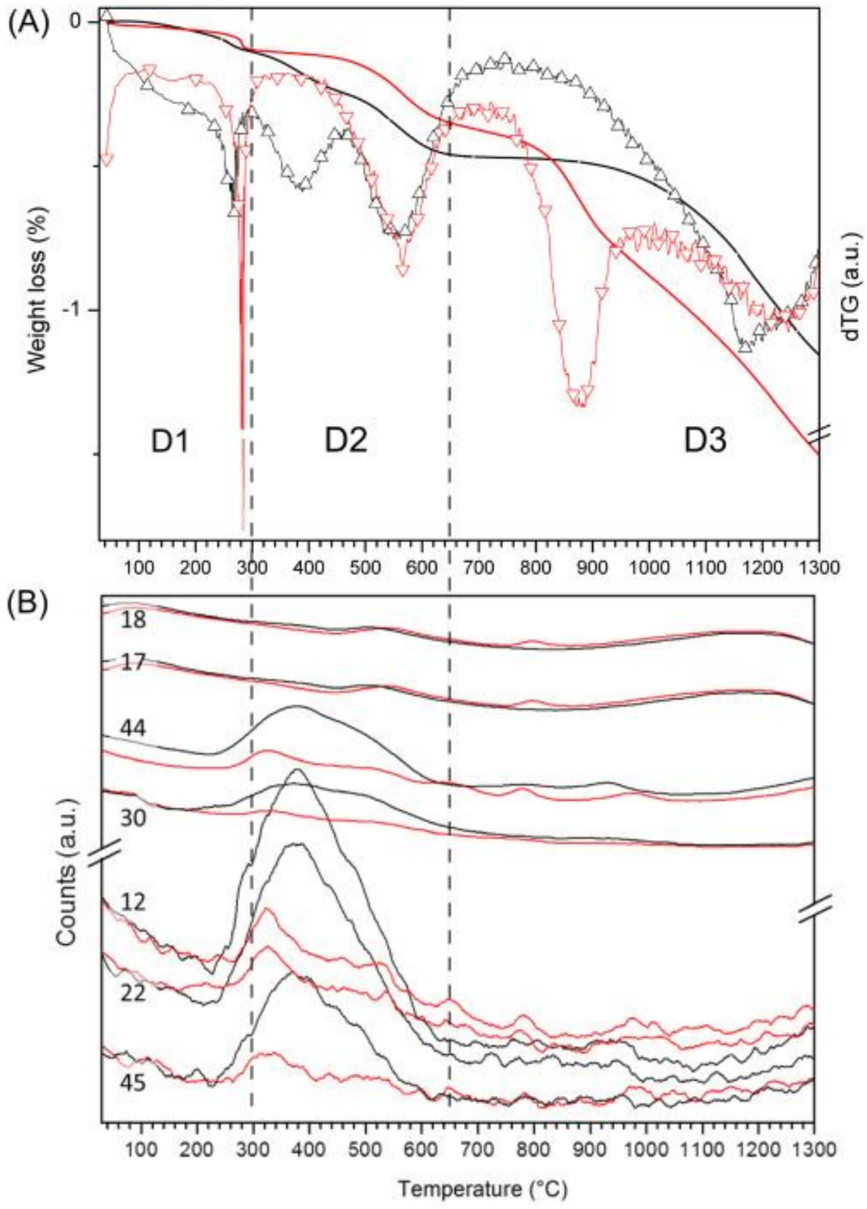

Figure 8: (A) Thermogravimetry (TG) curves of (black curve) SiHA-T pellet and (red curve) SiHA-BMP-2 pellet and derivatives of thermogravimetry curves (dTG) of (black up triangle) SiHA-T pellet and (red down triangle) SiHA-BMP-2 pellet. (B) Mass emission curves of (black curve) SiHA-T pellet and (red curve) SiHA-BMP-2 pellet.

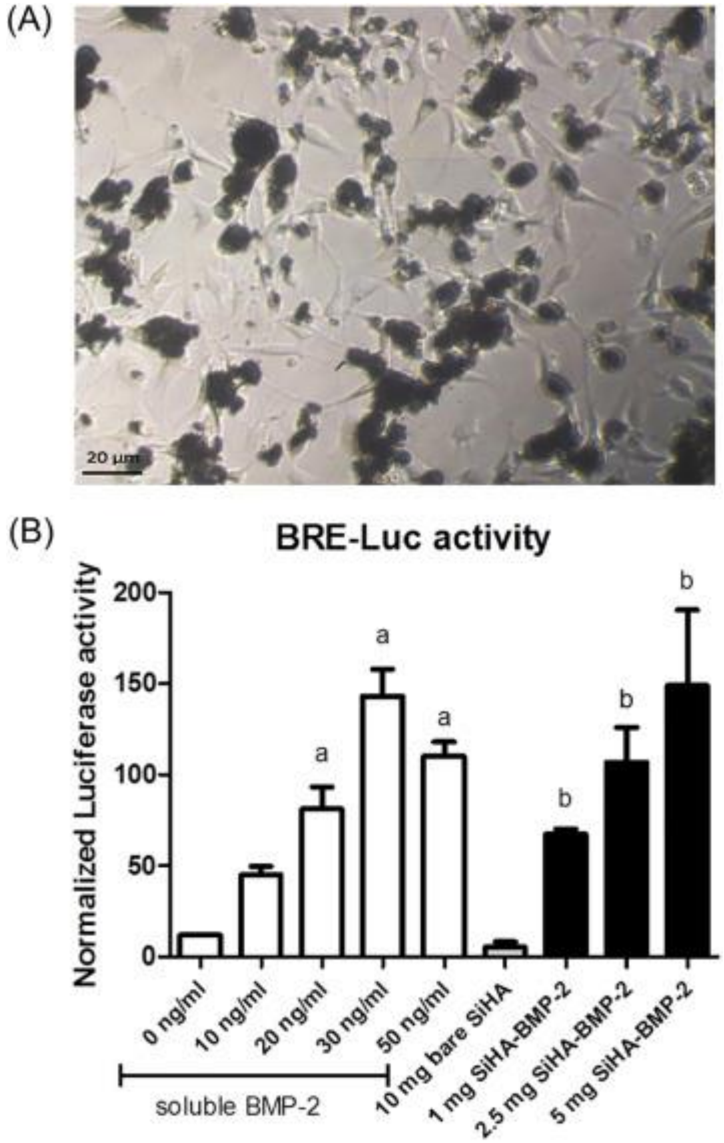

Figure 9: *In vitro* bioactivity of BMP-2 grafted onto SiHA spheres. (A) Observation of C3H10-BRE/Luc cells cultured with SiHA-BMP-2 spheres. (B) Quantification of the luciferase activity of C3H10-BRE/Luc cells cultured with bare (*i.e.* unfunctionalised) SiHA and SiHA-BMP-2 spheres for 24 h. For each condition, luciferase activity was normalized by the DNA content. (a) $p < 0.05$ as compared to the absence of BMP-2; (b) $p < 0.05$ as compared to bare spheres (one-way ANOVA).

Table 1. XPS survey atomic composition (at. %) of the surface of unfunctionalized and functionalized spheres. The absolute uncertainty on atomic percentage is 2%.

	Ca	**P**	**O**	**C**	**Si**	**N**	**S**	**Na**
SiHA	16	10	52	21	1	–	–	–
SiHA-T	6	4	35	39	8	8	–	–
SiHA-PEG	7	7	39	38	4	5	–	–
SiHA-BMP-2	11	8	53	16	1	2	–	9

Table 2. Experimental results of the XPS high-resolution analysis of N1s and C1s for SiHA-T, SiHA-PEG and SiHA-BMP-2 spheres.

		% Area		
C1*s* assignment	**Position (eV)**	**SiHA-T**	**SiHA-PEG**	**SiHA-BMP-2**
$\underline{C}H_x/\underline{C}-C$	285.2–285.3	69	50	59
$\underline{C}-O$	286.4–286.7	25	40	27
$\underline{C}=O/N-\underline{C}=O$	287.9–288.7	3	7	7
$O-\underline{C}=O$	289.3–289.4	3	3	7
N1*s* assignment				
$C-\underline{N}H_2$	399.6	87	–	–
$\underline{N}-C=O/O=C-\underline{N}-C=O$	400.1–400.2	–	62	70
$C-\underline{N}H_3^+ / O=C-\underline{N}H_2^+$-	401.3–401.6	13	38	30

Table 3. Molecular weights and assigned formulae of indexed organic fragments.

Organics and fragments	Organics and fragments formula	m/e
APTES	$NH_2(CH_2)_3Si(OCH_2CH_3)_3$	221
Amine chains	C_3H_8N, C_3H_7N, C_3H_6N, C_3H_5N, C_3H_4N, C_3H_3N, C_3H_2N, C_3HN, C_3N	58 to 50
	C_2H_6N, C_2H_5N, C_2H_4N, C_2H_3N, C_2H_2N, C_2HN, C_2N	44 to 38
	CH_4N, CH_3N, CH_2N, CHN, CN	30 to 26
	NH_3, NH_2, NH	17, 16, 15
	N_2, N	28, 14
Ethoxy chains	C_2H_5O, C_2H_4O, C_2H_3O, C_2H_2O, C_2HO, C_2O	45 to 40
	CH_2O, CHO, CO	30 to 28
Siloxane chains	C_2H_5OSi, C_2H_4OSi, C_2H_3OSi, C_2H_2OSi, C_2HOSi, C_2OSi	72 to 68
	CH_2OSi, CHOSi, COSi	58 to 56
	SiO	44
Silane chains	C_3H_6Si, C_3H_5Si, C_3H_4Si, C_3H_3Si, C_3H_2Si, C_3HSi, C_3Si	70 to 64
	C_2H_4Si, C_2H_3Si, C_2H_2Si, C_2HSi, C_2Si	56 to 52
	CH_2Si, CHSi, CSi	42 to 40
Alkyle chains	C_3H_6, C_3H_5, C_3H_4, C_3H_3, C_3H_2, C_3H, C_3	42 to 36
	C_2H_5, C_2H_4, C_2H_3, C_2H_2, C_2H, C_2	29 to 24
	CH_3, CH_2, CH, C	15 to 12
Carbone dioxide	$^{12}CO_2$, $^{13}CO_2$	44, 45
Water	H_2O, HO, O	18, 17, 16
Hydrogen	H	1